Nanoscale mapping of DNA dynamics reveals activity-driven genome organization in living human cells

Haitham A. Shaban[1,2] *, Roman Barth[1,3] and Kerstin Bystricky[1] *

1: Laboratoire de Biologie Moléculaire Eucaryote (LBME), Centre de Biologie Intégrative (CBI), CNRS; University of Toulouse, UPS; 31062 Toulouse; France; 2: Spectroscopy Department, Physics Division, National Research Centre, Dokki, Cairo, Egypt; 3: Present Address: Faculty of Applied Sciences, Delft University of Technology; 2628 CJ Delft; The Netherlands

* Correspondence: Email haitham.shaban@ibcg.biotoul.fr , kerstin.bystricky@ibcg.biotoul.fr

ABSTRACT

Principles of genome folding and their relationship to function depend on understanding conformational changes of the chromatin fiber. Analysis of bulk chromatin motion at high resolution is still lacking. We developed Hi-D, a method to quantitatively map DNA dynamics for every pixel simultaneously over the entire nucleus from real-time fluorescence images. Hi-D combines reconstruction of chromatin motion using computer vision and classification of local diffusion processes by Bayesian inference. We found that DNA dynamics in the nuclear interior are spatially organized into 0.3 – 3 μm domains of distinct types of diffusion was uncoupled from chromatin compaction. Reorganization of the network of dynamic domains between quiescent and active cells suggest that the microenvironment plays a predominant role in stochastic chromatin motion. Hi-D opens new perspectives towards understanding of chromatin organization placing global motion of nuclear molecules in the context of nuclear architecture.

INTRODUCTION

Spatial organization and dynamics of chromatin correlate with cell function and fate (Serizay and Ahringer 2018). In mammalian cells, chromosomes occupy territories whose localization is stable over the cell cycle although their positioning relative to each other and to other nuclear bodies, and degree of intermingling varies between cells(Cremer et al. 2015). Each chromosome contains dense, heterochromatin regions and open, euchromatin areas whose extent is indicative of cellular activity (Banerjee et al. 2006). Transitions within and between eu- and heterchromatin involve multiple levels of chromatin organization from nucleosome density, long-range looping and domain folding that adapt to and enable DNA processing (Fraser and Bickmore 2007). Structural models derived from contact and crosslinking frequencies(Lieberman-Aiden et al. 2009; Dixon et al. 2012; Beagrie et al. 2017) are consistent with the view that the genome is organized in compartments(Nora et al. 2012) but the true physical nature and localization of these compartments is not known. Understanding formation of nuclear substructures and even the folding of the nucleosome fiber itself requires imaging the behavior of chromatin in living cells. Tracking of labelled single DNA loci (Chubb et al. 2002; Levi et al. 2005; Chuang et al. 2006; Chen et al. 2013; Germier et al. 2017) or chromatin domains (Bornfleth et al. 1999; Nozaki et al. 2017) demonstrated that chromatin motion is highly heterogeneous at short time intervals. A few studies showed that chromatin motion was sub-diffusive, however, sparse loci are difficult to place in the context of global chromatin organization which is subject to highly complex dynamics (Di Pierro et al. 2018). Locally restricted genomic processes can also not be inferred from averaging motion over the entire nucleus (Zidovska et al. 2013; Shinkai et al. 2016).

To decipher the relationship between genome dynamics, organization and activity, we developed a new method, called Hi-D, to overcome the limitations of sparse and ensemble approaches for imaging dense structures such as chromatin and nuclear proteins. Hi-D, a combination of dense optical flow reconstruction to track the local motion of chromatin at sub-pixel accuracy in live cell

2

imaging(Shaban et al. 2018), and a Bayesian inference approach to precisely classify local types of diffusion. Biophysical properties such as diffusion coefficients and anomalous diffusion exponents were determined for each pixel and assigned to nuclear compartments. We present for the first time a two dimensional map of fluorescently labelled chromatin dynamics at sub pixel resolution down to 65 nm over the entire nucleus in living single cells. We examine the capacity to study dynamic changes of labelled chromatin in quiescent and stimulated cells. We find that in general, contrary to common belief, DNA compaction and dynamics do not necessarily correlate and strengthen the hypothesis that instead extrinsic mechanisms such as macromolecular crowding and association with the nuclear lamina dictate chromatin dynamics at local scales.

RESULTS

Hi-D determines and classifies DNA dynamics at nanoscale

We reconstructed trajectories of virtual particles from a series of conventional confocal fluorescence microscopy images analyzed by a dense Optical Flow method (Shaban et al. 2018) (supplementary note 1). First, we validated that MSD curves and derived diffusion constants were significantly greater in living than in formaldehyde fixed cells (Supplementary Figure 2). The type of diffusion characterizing each pixel's chromatin motion was determined in an unbiased manner using Bayesian inference to simultaneously test a set of common models to fit each MSD curve (Monnier et al. 2012). The five principal models are shown as a coloured map directly on the nucleus (Figure 1b right panel) (Methods section). This classification of local diffusion processes revealed that diffusion of DNA is highly heterogeneous throughout the nucleus presumably due to numerous mechanisms influencing chromatin fiber physical properties including molecular crowding and energetic processes such as active transport or chromatin remodeling during transcription.

We found that only a small fraction of trajectories displayed directed diffusion (Figure 1b), while the bulk of chromatin exhibited sub-diffusive behaviour. By examining a wide range of parameters governing these types of diffusion, our results suggest that chromatin diffusion can be adequately

3

described as anomalous (Supplementary note 2 and Supplementary Figure 4). Biophysical parameters calculated for each pixel (diffusion constant D, anomalous exponent α and drift velocity V) and presented in color-coded 2D heatmaps (Figure 1c) (Methods section) show islands of irregular shape and dimensions that contain fast diffusing DNA with large variations in the anomaly of DNA motion (Figure 1c). We determine that chromatin mobility groups spatially partition the nucleus into a network of domains.

Hi-D mapping resolves heterogeneous motion of chromatin independently of compaction

We investigated whether chromatin motion and compaction are correlated, because it is widely assumed that heterochromatin is less dynamic (Nozaki et al. 2017). Deconvolution of the distribution of diffusion constants revealed three subpopulations (Methods section) (Figure 2b). A distinct $100 -200\ nm$ peripheral rim of slow freely-diffusing DNA (D values $< 1.1\ \text{x}10^{-3}\ \mu\text{m}^2/\text{s}$) and reminiscent of lamin-associated domains (LADs)(Kind et al. 2013) colocalized with dense chromatin (Figure 2c,h). Inside the nucleus, a network of fast sub-diffusive areas of irregular dimensions spanning $0.3-3\ \mu m$ in diameter was imbedded in the bulk of moderately dynamic chromatin. Surprisingly, intra-nuclear heterochromatin domains and areas of these moderately sub-diffusive areas only overlapped partially in U2OS cells (Figure 2g, h). The analysis was confirmed on n=13 U2OS cells and similar results were obtained in MCF-7 cells (Supplementary Figure 6). These results reveal that chromatin dynamics are largely uncoupled from compaction.

Transcription status alters nuclear diffusion processes at the chromatin level

We assessed the effect of stimulating transcriptional activity on chromatin dynamics. Compared to serum-starved U2OS nuclei, average D decreased by nearly one order of magnitude for all three mobility groups upon addition of serum (Figure 3a). In serum-stimulated cells, sub-diffusive and super-diffusive regimes were strengthened (Figure 3b). The presence of a population with α close to 0.5 in both conditions was indicative of a Rouse-like chromatin fiber architecture (Hajjoul et al. 2013; Ghosh and Jost 2018). We hence hypothesize that the global decrease in D upon transcription

4

activation stems from factor binding to the chromatin fiber or viscoelastic properties of the microenvironment (Lucas et al. 2014) including non-chromatin nuclear bodies such as speckles(Kim et al. 2018). A subset of these activities could be involved in active processes including long-range interactions or transport resulting in apparent super-diffusion.

In serum starved cells, large variations of D are suggestive of a range of diffusion modes in the absence of DNA related activities (Figure 3c,d) and increased α (~0.75) in a large fraction of DNA further corroborates particle-like behavior of the fiber in a crowded solution(Banks and Fradin 2005). In contrast, upon serum stimulation anomalous diffusion (α ~0.33) was predominant and indicative of entangled polymers(Doi and Edwards 1988). Independence of D and α confirmed that compaction, chromatin mobility and forces hindering normal diffusion are not or only very weakly correlated (Supplementary Figure 7). Upon serum stimulation, reduced D again suggests that DNA-related processes hamper local chromatin diffusion and that α is altered due to functional reorganization of the chromatin fiber.

Single-cell biophysical property maps of genome conformation and behaviour

To concomitantly monitor position and distribution of the three mobility populations in quiescent and activated cells, we determined Hi-D maps for a single cell (Figure 4a, b). The low D population occupying ~6% of the nuclear area was invariant to transcriptional changes (Figure 4c). In contrast, upon serum stimulation, a large fraction of the fast moving population in quiescent cells was re-classified as intermediate mobility population with moderate changes in the mode of diffusion (Figure 4d). We conclude that decreased mobility results from a change in the microenvironment rather than from fiber folding.

Anomalous diffusion dominated across the entire nucleus ($0.3 \leq \alpha \leq 0.73$) forming a connected network which was reinforced in transcriptionally active nuclei (Figure 4f). Within this network, patches of highly anomalous (blue: < 0.3) and super-diffusive (red: $\alpha > 1$) motion segregated into distinct islands which became more fragmented upon serum stimulation (Figure 4g, h). Hi-D thus

5

reveals spatio-temporal changes in hindered diffusion of chromatin domains at high resolution in single cells. Further investigation may tell us if all or a subset of these physical domains correspond to the ones determined using Hi-C or GAM.

DISCUSSION

Hi-D is a single cell approach that enables tracking of dense structures such as chromatin and condensates directly and further classification of the highly heterogeneous underlying type of motion without losing active fluorophore density and with no need for prior experience in sophisticated labelling preparations or advanced microscopy (Manley et al. 2008). The information gain through image analysis afforded by Hi-D alleviates the incompatibility of conventional microscopy for nanoscale mapping of chromatin dynamic properties in living cells.

Hi-D analysis revealed three distinct populations of DNA diffusing in a comparable manner. The first, a slow mobility fraction at the nuclear rim, is reminiscent of lamina associated domains (LADs) (Kind et al. 2013) Decrease of mobility in the active state supports the hypothesis that LADs play an important role for attenuating transcription activity and of integrity of gene expression(Akhtar et al. 2013). Our analysis points out that although the periphery of nuclear chromatin in most cases is less mobile and largely connected to the existence of heterochromatin, it is independent of chromatin compaction levels. The intermediate and highly diffusive regimes were distributed in a mosaic-like pattern within the nucleus, with a small extent being nevertheless present at the nuclear periphery. Heterochromatin therefore does not exhibit low mobility in general, but may be divided into rigid elastic LAD chromatin with reduced mobility and a more viscous component. The extent of the third, highly mobile fraction which dominated chromatin behaviour in the quiescent state, decreased dramatically when cells were serum stimulated. This switch in chromatin mobility in distinct nuclear domains indicates changes in local molecular crowding which may result from accumulation of actors regulating gene expression (Ghamari et al. 2013; Cisse et al. 2013; Norred et al. 2018; Shaban et al. 2018). Heterogeneous chromatin motion arises due to irregular protein binding along the

chromosomes and can lead to thermodynamic or electrostatic self-organisation of nuclear compartments (Haddad et al. 2017; Sewitz et al. 2017). Local patches of large anomalous exponents indicate super-diffusive behaviour of chromatin which may result from loop extrusion by structural maintenance of chromosome (SMC) complexes (Vian et al. 2018; Ganji et al. 2018). Strikingly, quiescent cells show an increase of chromatin condensation by accumulation of the SMC complex condensin during quiescence entry (Swygert et al. 2018), which is indicative of dynamically active chromatin in quiescence. Furthermore, chromatin patches with $\alpha < 0.3$ and $\alpha > 1$ respectively correspond in size to one or a few TADs (Giorgetti et al. 2014). These two types of patches are present as a network within the general chromatin fraction governed by an anomalous exponent $0.3 < \alpha < 1$. This organization is in good agreement with the chromosome territory – interchromatin compartment model (Cremer et al. 2015). In conclusion, the combination of diffusion and anomalous exponent maps are complementary and provide new insights into chromatin organization and long-range interactions (active transport) during genomic processes.

We focus here on DNA, but Hi-D can be applied to real-time imaging of any fluorescent molecule to obtain comprehensive maps of their dynamic behavior in response to stimuli, inhibitors or disruptors of nuclear functions and integrity. Hi-D could be combined with tracking specific loci to zoom in on their environment. It will also be exciting to probe phase separating condensates to gain a better understanding of their physical nature(Erdel and Rippe 2018).

METHODS

Cell Culture. A Human U2OS osterosarcoma and MCF-7 cells (ATCC) were maintained in Dulbecco's modified Eagle's medium (DMEM) containing phenol red-free and DMED-12 (Sigma-Aldrich), respectively. Medium was supplemented with Glutamax containing 50 µg/ml gentamicin (Sigma-Aldrich), 10% Fetal bovine serum (FBS), 1 mM sodium pyruvate (Sigma-Aldrich) and G418 0.5 mg/ml

7

(Sigma-Aldrich) at 37°C with 5% CO2. Cells were plated for 24 h on 35 mm petri dishes with a #1.5 coverslip like bottom (μ-Dish, Ibidi, Biovalley) with a density of about 10^5 cells/dish.

Cell starvation and stimulation. For starvation mode, cells were incubated for 24 h at 37°C before imaging with serum-free medium (DMEM, Glutamax containing 50 μg/ml gentamicin, 1 mM sodium pyruvate, and G418 0.5 mg/ml). Just before imaging, cells were mounted in L-15 medium. For stimulation, 10% FBS was added to the L-15 medium for 10 minutes.

Chromatin staining. U2OS and MCF-7 cell lines were labelled by using SiR-DNA (SiR-Hoechst) kit (Spirochrome AG). For DNA was labelled as described in (Lukinavičius et al. 2015). Briefly, we diluted 1 mM stock solution in cell culture medium to concentration of 2 μM and vortexed briefly. On the day of the imaging, the culture medium was changed to medium containing SiR-fluorophores and incubated at 37°C for 30-60 minutes. Before imaging, the medium was changed to L-15 medium (Liebovitz's, Gibco) for live imaging.

Cell fixation: U2OS cells were washed with a pre-warmed (37 °C) phosphate buffered saline (PBS) and followed by fixation with 4% (vol/vol) Paraformaldehyde in PBS for 10-20 min at room temperature. Imaging movies were recorded at room temperature in PBS, after washing the cells with PBS (three times, 5 min per each).

Imaging: Cells were placed in a 37 °C humid incubator by controlling the temperature and CO2 flow using H201- couple with temperature and CO2 units. Live chromatin imaging was acquired using a DMI8 inverted automated microscope (Leica Microsystems) featuring a confocal spinning disk unit (CSU-X1-M1N, Yokogawa). Integrated laser engine (ILE 400, Andor) was used for excitation with a selected wavelength of 647 nm and 140mW as excitation power. A 100x oil immersion objective (Leica HCX-PL-APO) with a 1.4 NA was chosen for a high resolution imaging. Fluorescence emission of the SiR–Hoechst was filtered by a single-band bandpass filter (FF01-650/13-25, Semrock, Inc.). Image series of 150 frames (5 fps) were acquired using Metamorph software (Molecular Devices), and

8

detected using sCMOS cameras (ORCA-Flash4.0 V2) and (1×1 binning), with sample pixel size of 65 nm.

All series were recorded at 37°

Image processing

Denoising. Raw images were denoised using non-iterative bilateral filtering (Tomasi and Manduchi 1998). While Gaussian blurring only accounts for the spatial distance of a pixel and its neighbourhood, bilateral filtering additionally takes the difference in intensity values into account and is therefore an edge-preserving method. Abrupt transitions from high- to low-intensity regions (e.g. heterochromatin to euchromatin) are not over-smoothed.

MSD analysis and model selection by using Bayesian inference

In order to carry out a MSD analysis locally, the spatial dependency of the Mean Squared Displacement (MSD) can be written explicitly:

$$\text{MSD}(\vec{r}_0, \tau) = \langle |\vec{\xi}_{r_o}(t + \tau) - \vec{\xi}_{r_0}(t)|^2 \rangle_t,$$

where $\vec{\xi}_{r_0}(t)$ is the position at time t of a virtual particle with initial position $\vec{r}_0$, $\tau = \{\Delta t, 2\Delta t, \dots, (N-1)\Delta t\}$ are time lags where Δt is the time difference between subsequent images and the average $<\cdot>_t$ is taken over time. The resulting MSD is a function of the particle's initial position $\vec{r}_0$ and the time lag τ.

MSD models: The MSD can be expressed analytically for anomalous diffusion (DA), confined diffusion (DR) and directed motion (V) in two dimensions as

$$MSD_{DA}(\tau) = 4D\tau^{\alpha} \tag{1}$$

$$MSD_{DR}(\tau) = R_C^2 \left(1 - e^{-\frac{4D\tau}{R_C^2}} \right) \tag{2}$$

$$MSD_V(\tau) = v^2\tau^2 \tag{3}$$

9

where D is the particles diffusion coefficient, α is its anomalous exponent, v its velocity and R_C is the radius of a sphere within the particle is confined(Saxton and Jacobson 1997). The case $\alpha = 1$ is known as free diffusion, $0 < \alpha < 1$ corresponds to anomalous diffusion and $1 < \alpha \leq 2$ corresponds to superdiffusion. Additionally to eq. (1)-(3), different types of motion can appear overlaying, resulting in a linear combination of the equations above. For example, confined motion can be superimposed on an underlying drift and the resulting MSD reads $MSD_{DRV}(\tau) = MSD_{DR}(\tau) + MSD_V(\tau)$. The abbreviations used in this study correspond are summarized in Table 1. As experimental data is usually subject to noise, a constant offset o is added to every model.

Abbreviation	Model	Formula
D	Free diffusion	$MSD_D(\tau) = 4D\tau + o$
DA	Anomalous diffusion	$MSD_{DA}(\tau) = 4D\tau^{\alpha} + o$
V	Drift	$MSD_V(\tau) = v^2\tau^2 + o$
DV	Free diffusion + drift	$MSD_{DV}(\tau) = 4D\tau + v^2\tau^2 + o$
DAV	Anomalous diffusion + drift	$MSD_{DAV}(\tau) = 4D\tau^{\alpha} + v^2\tau^2 + o$

Table 1: Overview over possible Mean Squared Displacement models

MSD model selection: The MSD is calculated for every pixel independently, resulting in a space- and time lag-dependent MSD. It is known that living cells can behave largely heterogeneous(Banerjee et al. 2006; Dickerson et al. 2016). Ad-hoc, it is not known which particle undergoes which kind of diffusion. Fitting a MSD curve with a wrong model might result in poor fits and highly inaccurate determination of the mentioned parameters. For this reason, we use a Bayesian inference approach to test different models for any given MSD curve as proposed by Monnier *et al.*(Monnier et al. 2012). Given the data $Y = \{Y_1, \ldots, Y_n\}$ and K model candidates $M = \{M_1, \ldots, M_K\}$, each with its own (multidimensional) parameter set $\theta = \{\theta_1, \ldots, \theta_K\}$, we want to find the model $M_k(Y, \theta_k)$ such that the probability that $M_k(Y, \theta_k)$ describes the data, given the set of models to test, is maximal. By Bayes' theorem, the probability for each model is given by

$$P(M_k|Y) = \frac{P(Y|M_k)P(M_k)}{P(Y)}$$

If there is no reason to prefer one model over the other, the prior probability of each model $P(M_k)$ is equal. The parameter set which is used to describe the data, given a fixed model, strongly influences the probability. Therefore, it is crucial to estimate the optimal parameters for every model in order to calculate the model probabilities. The probability that the data Y is observed, given the model M_k described by the model function $M_k(x; \theta_k)$ and any parameter set θ_k is approximated by a general multivariate Gaussian function (Seber and Wild 2003)

$$P(Y|\theta_k, M_k) = \frac{1}{\sqrt{(2\pi)^n \det(C)}}$$
$$\cdot \exp\left\{-\frac{1}{2}[Y - M_k(x; \theta_k)]^T \cdot C^{-1} \cdot [Y - M_k(x; \theta_k)]\right\}$$

where C is the empirical covariance matrix of the data and the prefactor is a normalizing factor. This equation has an intuitive meaning. Assume we test a model M_k parametrized by θ_k to find out if it describes the data Y. The exponential function consists of the term $[Y - M_k(x; \theta_k)]$, i.e. the residuals of the data and the describing model. If the residuals are small, i.e. the model describes the data well, the exponent is small and the probability $P(Y|\theta_k, M_k)$ seeks 1. On the other hand, the worse the fit, the greater the resulting residuals and the probability seeks asymptotically to 0. The factor C^{-1} accounts for the covariance in the data. The covariance matrix for a set of MSD curves normally shows large values for large time lags as the uncertainty increases and MSD curves diverge. The covariance matrix implicitly introduces a weight to the data, which is small for large variances and large where the data spreads little. This fact avoids cutting of the MSD curve after a specific number of time lags, but instead includes all available time lags weighted by the covariance matrix. The approach is illustrated in (Supplementary Figure 3b) with the covariance matrix exemplary shown in the inset. In case of uncorrelated errors, non-diagonal elements are zero, but the approach keeps its validity(He et al. 2012) and follows an ordinary least-squares regression.

Given the best estimate of the parameter set for a model, the model and its corresponding parameters are chosen so that their probability to describe the data is maximal: $\hat{\theta}_{k,MLE} = \arg\max_{\theta_k} P(Y|\theta_k, M_k)$.

It has to be stressed that values of the anomalous exponent scatter around 1, but do not assume the value 1. This is due to the model selection procedure, selecting the simplest model consisting with the data. In case that the underlying motion is well described by free diffusion, α is inherently set to 1 and classified as free diffusion rather than anomalous diffusion. The descriptions of free diffusion or anomalous diffusion with $\alpha = 1$ are equivalent, but the free diffusion model contains one parameter less and is therefore preferred leading to abundance of α values close to 1 in the parameter maps and histograms. To carry out the MSD analysis locally, we choose to take the 3x3 neighborhood of a pixel, detect possible outliers therein by the interquartile range criterion (Rousseeuw and Croux 1993) and calculate the error covariance matrix of the data within the pixel's neighborhood. The restriction to a single pixel and its neighborhood allows us to carry out the MSD analysis of trajectories locally, in contrast to an ensemble MSD in previous studies (Zidovska et al. 2013), revealing only average information over many trajectories. The choice of a 3x3 window is reasonable with regard to the equivalently chosen filter size in the Optical Flow estimation. The flow field in this region is therefore assumed to be sufficiently smooth. All calculations, except for the General Mixture Model analysis, were carried out using MATLAB (MATLAB Release 2017a, The MathWorks, Inc., Natick, Massachusetts, United States) on a 64-bit Intel Xeon CPUE5-2609 1.90 GHz workstation with 64 GB RAM and running Microsoft Windows 10 Professional.

Deconvolution of sub-populations

Regarding especially the distribution of the diffusion coefficient, an analytical expression can be found assuming that the diffusion coefficient was calculated from a freely diffusing particle ($\alpha = 1$)(Vrljic et al. 2002). However, we find anomalous diffusion to a large extent in our data (e.g. Figure 2e, f and Figure 4d) and, to our knowledge, an analytical expression cannot be found for distributions of

12

anomalous exponent, radius of confinement and drift velocity. We therefore aim to deconvolve the parameter sets in a rather general manner, for which we use a General Mixture model (GMM), a probabilistic model composed of multiple distributions and corresponding weights. We describe each data point as a portion of a normal or log-normal distribution described by

$$f_N(Y|\mu,\sigma^2) = \frac{1}{\sqrt{2\pi}\sigma} e^{-\frac{(Y-\mu)^2}{2\sigma^2}} \text{ and}$$

$$f_L(Y|\mu,\sigma^2) = \frac{1}{Y\sqrt{2\pi}s} e^{-\frac{(\ln(Y)-m)^2}{2s^2}},$$

respectively. The logarithmic mean m and standard deviation s are related to the mean and standard deviation of the normal distribution via (Mood et al. 1974)

$$\mu = \exp\left(m + \frac{s^2}{2}\right)$$

$$\sigma^2 = \exp(2m + s^2)(e^{\sigma^2} - 1)$$

We consider up to three subpopulations to be found in our data and model the total density estimate as a superposition of one, two or three subpopulations, i.e. the Mixture Model reads

$$f_{GMM}(Y) = \sum_k w_k \, f_k\big(Y|\mu_k,\sigma_k^2\big)$$

for both normal and log-normal distributions, where to sum goes to 1, 2 or 3. The variable w_k describes the weights for each population (or component), which satisfy $0 \leq w_k \leq 1$ and sum up to unity. The weights of each component are directly proportional to the area of the histogram covered by this component and therefore its existence in the data set.

General Mixture Model analysis

Let $Y = \{Y_1, ..., Y_n\}$ denote n data points. For the scope of this description, assume Y to be a one-dimensional variable. Further assume that the data cannot be described by a single distribution, but by a mixture of distributions. A deconvolution of the data into sub-populations faces the following problem: Given a label for each data point, denoting the affiliation to a population, one could group corresponding data points and find the parameters of each population separately using a maximum

13

likelihood estimation or other methods. On the other hand, if we had given the model parameters for each population, labels could in principle be inferred from the likelihood of a data point being described by a population or another. The problem can be formulated by Bayes' rule (M indicates model, D indicates data)

$$P(M|D)P(D) = P(D|M)P(M).$$

Here, $P(M|D)$ is the posterior probability of the model given the data, which is the aim to calculate. We assign a data point to the component, which maximizes $P(M|D)$. The probability to observe the data given a model is described by $P(D|M)$, i.e. the likelihood function. $P(M)$ is the prior for the models to be chosen from. In our case, we have no prior beliefs on the models (all models are equally likely) such that $P(M)$ is uniform. Lastly, the probability $P(D)$ does not depend on the models and can therefore be dropped.

Unfortunately, neither labels, that is $P(M|D)$, nor model parameters and weights are known a priori. The problem can be approached by an Expectation-Maximization (EM) scheme: Without any prior beliefs about the data distribution, one starts with a simple estimate of model parameters, e.g. a k-means clustering estimate and iterates subsequently between the two following steps until convergence:

Expectation step: Calculation of the probability that the component with the current parameter estimate generated the sample, i.e. $P(D|M)$.

Maximization step: Update the current parameter estimate for each component by means of a weighted maximum likelihood estimate, where the weight is the probability that the component generated the sample.

We illustrate the results of the EM algorithm exemplary in Supplementary Figure 5. From the input data (Supplementary Figure 5a), represented as histogram, both the likelihood $P(D|M)$ (Supplementary Figure 5b) and the posterior (Supplementary Figure 5c) is obtained. The sum of sub-populations corresponds to the overall probability distribution (shown in black) with different model

14

parameters and weights found by maximizing the likelihood function. The posterior describes the probability of data points to fall under each population, i.e. $\sum_k P(M_k|D) = 1$. The data points are assigned to those population, for which $P(M_k|D)$ is maximum, resulting in labeled data. The labels are subsequently mapped in two dimensions, visualizing spatial correspondence of slow, intermediate and fast sub-populations (Supplementary Figure 5d). The GMM analysis is carried out using the pomegranate machine learning package for probabilistic modeling in Python (Schreiber 2017).

Selection of subpopulations by the Bayesian Information Criterion (BIC)

A priori, it is not unambiguously clear from how many populations the data is sampled and which form the subpopulations take. We therefore assess the suitability of each model by means of the Bayesian Information Criterion (BIC), which is calculated by(Schwarz 1978)

$$BIC = -2\ln(\hat{L}) + p \, ln(n), \tag{3}$$

where $\hat{L}$ is the maximum likelihood of the maximum likelihood estimation (MLE) estimate, p denotes the number of parameters in the model and n is the number of data points used for the fit. Among a family of models, the one with the lowest BIC is considered to describe the data best, taking into account competing complexity of models. A large likelihood of a model favors it to describe the data well, while on the other hand the model is penalized if many parameters are involved in the model by the second term in (3). Therefore, the BIC prevents overfitting. In order to judge which model is appropriate for our data, we tested all considered models for each histogram and assessed the optimal model by means of the BIC. The fraction of all histograms which described best by one of the six models considered is given in Supplementary Table 2. Based on the objective judgement of the fit using the BIC, we chose for each parameter the model which best describes the largest fraction of histograms (**Error! Reference source not found.**, bold cells).

	Normal distribution			Log-normal distribution		
#populations	1	2	3	1	2	3
D	0.01	0.01	0.06	0.01	0.40	**0.51**
α	0	0.05	**0.68**	0.02	0.03	0.22

Table 2: Fraction of histograms over all parameters best described by one of the six models considered. The highest fraction is shown in bold.

SUPPLEMENTARY INFORMATION

The Supplementary Information contains details on the conversion from flow fields to trajectories, a detailed discussion on the distinction of confined and anomalous diffusion and the usage of the Bayesian Information Criterion in testing the number of shape of sub-populations present in our data.

ACKNOWLEDGMENTS

AUTHOR CONTRIBUTIONS

H.A.S. conceived the method, performed the experimental work, developed the data processing algorithm and analyzed the data; R.B. wrote the code, developed the data processing algorithm and analyzed the data; K. B. funded the research; H.A.S. and K. B. interpreted the results; H.A.S., R. B. and K. B. wrote the manuscript.

CONFLICT OF INTEREST

The authors declare no competing financial interests.

REFERENCES

Akhtar W, De Jong J, Pindyurin A V., Pagie L, Meuleman W, De Ridder J, Berns A, Wessels LFA, Van Lohuizen M, Van Steensel B. 2013. Chromatin position effects assayed by thousands of reporters integrated in parallel. *Cell* **154**: 914–927.

Banerjee B, Bhattacharya D, Shivashankar G V. 2006. Chromatin structure exhibits spatio-temporal heterogeneity within the cell nucleus. *Biophys J* **91**: 2297–2303.

Banks DS, Fradin C. 2005. Anomalous diffusion of proteins due to molecular crowding. *Biophys J* **89**: 2960–2971.

Beagrie RA, Scialdone A, Schueler M, Kraemer DCA, Chotalia M, Xie SQ, Barbieri M, De Santiago I, Lavitas LM, Branco MR, et al. 2017. Complex multi-enhancer contacts captured by genome architecture mapping. *Nature* **543**: 519–524.

Bornfleth H, Edelmann P, Zink D, Cremer T, Cremer C. 1999. Quantitative motion analysis of subchromosomal foci in living cells using four-dimensional microscopy. *Biophys J* **77**: 2871–86.

Chen B, Gilbert L a, Cimini B a, Schnitzbauer J, Zhang W, Li G-W, Park J, Blackburn EH, Weissman JS, Qi LS, et al. 2013. Dynamic imaging of genomic loci in living human cells by an optimized CRISPR/Cas system. *Cell* **155**: 1479–91. http://www.ncbi.nlm.nih.gov/pubmed/24360272.

Chuang CH, Carpenter AE, Fuchsova B, Johnson T, de Lanerolle P, Belmont AS. 2006. Long-Range Directional Movement of an Interphase Chromosome Site. *Curr Biol* **16**: 825–831.

Chubb JR, Boyle S, Perry P, Bickmore WA. 2002. Chromatin motion is constrained by association with nuclear compartments in human cells. *Curr Biol* **12**: 439–445.

Cisse II, Izeddin I, Causse SZ, Boudarene L, Senecal A, Muresan L, Dugast-Darzacq C, Hajj B, Dahan M, Darzacq X. 2013. Real-time dynamics of RNA polymerase II clustering in live human cells. *Science (80-)* **341**: 664–667.

Cremer T, Cremer M, Hübner B, Strickfaden H, Smeets D, Popken J, Sterr M, Markaki Y, Rippe K, Cremer C. 2015. The 4D nucleome: Evidence for a dynamic nuclear landscape based on co-aligned active and inactive nuclear compartments. *FEBS Lett* **589**: 2931–2943.

Di Pierro M, Potoyan DA, Wolynes PG, Onuchic JN. 2018. Anomalous diffusion, spatial coherence, and viscoelasticity from the energy landscape of human chromosomes. *Proc Natl Acad Sci* **115**:

7753–7758. http://www.pnas.org/lookup/doi/10.1073/pnas.1806297115.

Dickerson D, Gierliński M, Singh V, Kitamura E, Ball G, Tanaka TU, Owen-Hughes T. 2016. High resolution imaging reveals heterogeneity in chromatin states between cells that is not inherited through cell division. *BMC Cell Biol* **17**.

Dixon JR, Selvaraj S, Yue F, Kim A, Li Y, Shen Y, Hu M, Liu JS, Ren B. 2012. Topological domains in mammalian genomes identified by analysis of chromatin interactions. *Nature* **485**: 376–380.

Doi M, Edwards SF. 1988. *The Theory of Polymer Dynamics*. Clarendon Press.

Erdel F, Rippe K. 2018. Formation of Chromatin Subcompartments by Phase Separation. *Biophys J* **114**: 2262–2270.

Fraser P, Bickmore W. 2007. Nuclear organization of the genome and the potential for gene regulation. *Nature* **447**: 413–417.

Ganji M, Shaltiel IA, Bisht S, Kim E, Kalichava A, Haering CH, Dekker C. 2018. Real-time imaging of DNA loop extrusion by condensin. *Science (80-)* **360**: 102–105.

Germier T, Kocanova S, Walther N, Elien Bancaud A, Shaban HAHA, Sellou H, Politi AZAZ, Ellenberg J, Gallardo F, Bystricky K, et al. 2017. Real-Time Imaging of a Single Gene Reveals Transcription-Initiated Local Confinement. *Biophys J* **113**: 1383–1394.

Ghamari A, van de Corput MPC, Thongjuea S, van Cappellen WA, van Ijcken W, van Haren J, Soler E, Eick D, Lenhard B, Grosveld FG. 2013. In vivo live imaging of RNA polymerase II transcription factories in primary cells. *Genes Dev* **27**: 767–77. http://genesdev.cshlp.org/cgi/doi/10.1101/gad.216200.113%5Cnhttp://genesdev.cshlp.org/content/27/7/767.abstract%0Ahttp://www.ncbi.nlm.nih.gov/pubmed/23592796%0Ahttp://www.pubmedcentral.nih.gov/articlerender.fcgi?artid=PMC3639417.

Ghosh SK, Jost D. 2018. How epigenome drives chromatin folding and dynamics, insights from efficient coarse-grained models of chromosomes ed. S. Zhong. *PLOS Comput Biol* **14**: e1006159.

Giorgetti L, Galupa R, Nora EP, Piolot T, Lam F, Dekker J, Tiana G, Heard E. 2014. Predictive polymer modeling reveals coupled fluctuations in chromosome conformation and transcription. *Cell* **157**: 950–963.

Haddad N, Jost D, Vaillant C. 2017. Perspectives: using polymer modeling to understand the formation and function of nuclear compartments. *Chromosom Res* **25**: 35–50.

Hajjoul H, Mathon J, Ranchon H, Goiffon I, Mozziconacci J, Albert B, Carrivain P, Victor JM, Gadal O, Bystricky K, et al. 2013. High-throughput chromatin motion tracking in living yeast reveals the flexibility of the fiber throughout the genome. *Genome Res* **23**: 1829–1838.

He J, Guo S-M, Bathe M. 2012. Bayesian approach to the analysis of fluorescence correlation spectroscopy data I: theory. *Anal Chem* **84**: 3871–9.

http://pubs.acs.org/doi/abs/10.1021/ac2034369%5Cnpapers2://publication/doi/10.1021/ac20 34369%5Cnhttp://www.ncbi.nlm.nih.gov/pubmed/22423978.

Kim J, Han KY, Khanna N, Ha T, Belmont AS. 2018. Nuclear speckle fusion via long-range directional motion regulates the number and size of speckles. *bioRxiv* 347955. https://www.biorxiv.org/content/early/2018/06/15/347955.

Kind J, Pagie L, Ortabozkoyun H, Boyle S, De Vries SS, Janssen H, Amendola M, Nolen LD, Bickmore WA, Van Steensel B. 2013. Single-cell dynamics of genome-nuclear lamina interactions. *Cell* **153**: 178–192.

Levi V, Ruan Q, Plutz M, Belmont AS, Gratton E. 2005. Chromatin Dynamics in Interphase Cells Revealed by Tracking in a Two-Photon Excitation Microscope. *Biophys J* **89**: 4275–4285.

Lieberman-Aiden E, van Berkum NL, Williams L, Imakaev M, Ragoczy T, Telling A, Amit I, Lajoie BR, Sabo PJ, Dorschner MO, et al. 2009. Comprehensive Mapping of Long-Range Interactions Reveals Folding Principles of the Human Genome. *Science (80-)* **326**: 289–293. http://www.sciencemag.org/cgi/doi/10.1126/science.1181369.

Lucas JS, Zhang Y, Dudko OK, Murre C. 2014. 3D trajectories adopted by coding and regulatory DNA elements: First-passage times for genomic interactions. *Cell* **158**: 339–352.

Lukinavičius G, Blaukopf C, Pershagen E, Schena A, Derivery E, Gonzalez-gaitan M, Este ED, Hell SW, Gerlich DW, Johnsson K. 2015. A far-red DNA stain for live-cell nanoscopy. *Nat Commun* **61**: 3–5. http://dx.doi.org/10.1038/ncomms9497.

Manley S, Gillette JM, Patterson GH, Shroff H, Hess HF, Betzig E, Lippincott-Schwartz J. 2008. High-density mapping of single-molecule trajectories with photoactivated localization microscopy. *Nat Methods* **5**: 155–157.

Monnier N, Guo S-M, Mori M, He J, Lénárt P, Bathe M. 2012. Bayesian approach to MSD-based analysis of particle motion in live cells. *Biophys J* **103**: 616–26. http://www.ncbi.nlm.nih.gov/pubmed/22947879%5Cnhttp://www.pubmedcentral.nih.gov/arti clerender.fcgi?artid=PMC3414897.

Mood AM, Graybill FA, Boes DC. 1974. Introduction to the Theory of Statistics. *Book* **3**: 540–541.

Nora EP, Lajoie BR, Schulz EG, Giorgetti L, Okamoto I, Servant N, Piolot T, Van Berkum NL, Meisig J, Sedat J, et al. 2012. Spatial partitioning of the regulatory landscape of the X-inactivation centre. *Nature* **485**: 381–385.

Norred SE, Caveney PM, Chauhan G, Collier LK, Collier CP, Abel SM, Simpson ML. 2018. Macromolecular Crowding Induces Spatial Correlations That Control Gene Expression Bursting Patterns. *ACS Synth Biol* **7**: 1251–1258. https://doi.org/10.1021/acssynbio.8b00139.

Nozaki T, Imai R, Tanbo M, Nagashima R, Tamura S, Tani T. 2017. Dynamic Organization of Chromatin

Domains Revealed by Super-Resolution Live-Cell Imaging. *Mol Cell* **10**: 1–12. http://dx.doi.org/10.1016/j.molcel.2017.06.018.

Peacock J a. 1983. Two-dimensional goodness-of-fit testing in astronomy. *Mon Not R Astron Soc* **202**: 615.

Rousseeuw PJ, Croux C. 1993. Alternatives to the Median Absolute Deviation. *J Am Stat Assoc* **88**: 1273–1283.

Saxton MJ, Jacobson K. 1997. Single-particle tracking: applications to membrane dynamics. *Annu Rev Biophys Biomol Struct* **26**: 373–399.

Schreiber J. 2017. Pomegranate: fast and flexible probabilistic modeling in python.

Schwarz G. 1978. Estimating the Dimension of a Model. *Ann Stat* **6**: 461–464.

Seber GAF, Wild CJ. 2003. *Nonlinear Regression*.

Serizay J, Ahringer J. 2018. ScienceDirect Genome organization at different scales : nature , formation and function. *Curr Opin Cell Biol* **52**: 145–153.

Sewitz SA, Fahmi Z, Aljebali L, Bancroft J, Brustolini OJB, Saad H, Goiffon I, Varnai C, Wingett S, Wong H, et al. 2017. Heterogeneous chromatin mobility derived from chromatin states is a determinant of genome organisation in S. cerevisiae. *bioRxiv* 106344. https://www.biorxiv.org/content/early/2017/03/02/106344.full.pdf+html.

Shaban HA, Barth R, Bystricky K. 2018. Formation of correlated chromatin domains at nanoscale dynamic resolution during transcription. *Nucleic Acids Res* **46**: e77. http://dx.doi.org/10.1093/nar/gky269.

Shinkai S, Nozaki T, Maeshima K, Togashi Y. 2016. Dynamic Nucleosome Movement Provides Structural Information of Topological Chromatin Domains in Living Human Cells. *PLoS Comput Biol* **12**.

Swygert SG, Kim S, Wu X, Fu T, Hsieh T-H, Rando OJ, Eisenman RN, Schendure J, McKnight JN, Tsukiyama T. 2018. Condensin-dependent chromatin condensation represses transcription globally during quiescence. *bioRxiv* 320895. https://www.biorxiv.org/content/early/2018/05/12/320895?utm_source=dlvr.it&utm_medium=twitter.

Tomasi C, Manduchi R. 1998. Bilateral Filtering for Gray and Color Images. *Proc 1998 IEEE Int Conf Comput Vis*.

Vian L, Pękowska A, Rao SSP, Kieffer-Kwon K-R, Jung S, Baranello L, Huang S-C, El Khattabi L, Dose M, Pruett N, et al. 2018. The Energetics and Physiological Impact of Cohesin Extrusion. *Cell* **173**: 1165–1178.e20. http://dx.doi.org/10.1016/j.cell.2018.03.072.

Vrljic M, Nishimura SY, Brasselet S, Moerner WE, McConnell HM. 2002. Translational diffusion of

individual class II MHC membrane proteins in cells. *Biophys J* **83**: 2681–2692.

Wachsmuth M, Knoch TA, Rippe K. 2016. Dynamic properties of independent chromatin domains measured by correlation spectroscopy in living cells. *Epigenetics and Chromatin* **9**: 1–20.

Zidovska A, Weitz D a, Mitchison TJ. 2013. Micron-scale coherence in interphase chromatin dynamics. *Proc Natl Acad Sci U S A* **110**: 15555–60.

Figure Legends

Figure 1: Hi-D enables spatially resolved mapping of genome dynamic properties at nanoscale resolution in living cells. Workflow: **a)** A series of N=150 confocal microscopy images acquired at 5 fps (left) (here SiR DNA stained living U2OS cells). Dense optical flow was applied to define (N-1) flow fields of the images (center, color coded) based on fluorescence intensity of each pixel (size = 65 nm). Individual trajectories are reconstructed over the duration of acquisition (right). **b)** MSD model selection (left): Trajectories of a 3x3 neighborhood of every pixel are used to calculate a mean MSD curve and its corresponding covariance matrix. By a Bayesian inference approach, the type of diffusion fitting each individual curve is chosen (free diffusion (D), anomalous diffusion (DA), directed motion (V) or a combination (DV) or (DAV). The spatial distribution of the selected models for each pixel is shown as a color map. **c)** Maps of biophysical parameters (D, α and V) extracted from the best describing model per pixel reveal local dynamic behavior of DNA in large domains.

Figure 2: DNA dynamic properties and chromatin compaction are uncoupled. a) Fluorescence image from a time-lapse video of a SiR stained U2OS nucleus. **b)** Color-coded Bayesian inference selected models for each pixel. The color code is shown in the inset. **c)** Heat-maps of diffusion coefficient distribution of DNA motion and **d)** anomalous exponent. One representative nucleus is shown (n=13 analyzed individually). White pixels inside the nucleus correspond to pixels for which either no signal intensity was observed (such as nucleoli) or no MSD model carrying a diffusion coefficient was chosen (such as purely ballistic motion). **e)** The diffusion coefficient is measured relative to the distance to the nearest periphery (upper panel) or nucleolus boundary (lower panel) pixel by a binned Euclidean distance transform (mean value +/- standard deviation). **f)** Data points of the diffusion coefficient and **g)** anomalous exponents are represented as histogram and the overall distribution (black line) and deconvolved into low, intermediate and high distributions by a probabilistic General Mixture Model (GMM) (population distributions shown in colored lines respectively; Methods section). Mobility groups partitioning DNA dynamics within the nucleus can be classified into one of these populations and mapped back into two dimensions for **h)** diffusion coefficient and **i)** anomalous exponent respectively. **j)** Relative share of each model in the three populations corresponding to the diffusion coefficient for each pixel. **k)** Spatial classification of signal intensity into eu- and heterochromatin(Wachsmuth et al. 2016) and **l)** overlay with the diffusion populations found in h) as well as **m)** the anomalous exponent found in i). Black solid lines corresponding to heterochromatin region boundaries include intermediate and high mobility groups.

22

Figure 3: Biophysical properties of chromatin are sensitive to genome activity. Quantification of transcription induced dynamic parameter changes in actively transcribing cells (+ Serum) compared to quiescent (- Serum) U2O2 cells (n=13). **a)** Mean diffusion coefficients (n=13) of all three mobility groups are reduced; red, gold and yellow violin plots represent slow, intermediate and fast diffusion coefficient constants respectively. **b)** Changes in anomalous exponents. Statistical significance for a-b) assessed by a Friedman test (*: $p < 0.05$, **: $p < 0.01$, ***: $p < 0.001$). **c)** Parameter values and corresponding population weights from GMM are represented as two dimensional kernel density estimates (circles, diamonds and squares correspond to data points of the low, intermediate and high population respectively; surrounded markers indicate the population mean over all nuclei. **d)** Anomalous exponent as in c). Statistical significance for c-d) shown in Supplementary Figure 7 and assessed by a multivariate extension of the Kolmogorov-Smirnov test(Peacock 1983).

Figure 4: Intra-nuclear networks of anomalous diffusion are modulated by transcription. **a)** Spatial distribution of GMM defined mobility groups for the diffusion coefficient for quiescent (a) and **b)** actively transcribing U2OS cells. **c) Serum induced transcription activity** reduces the high mobility group at the expense of the intermediary one. **d) Motion classification of each mobility group is insensitive to serum addition.** For each population in a-b), the relative share of chosen MSD models is represented as stacked histogram for quiescent (left bars) and actively transcribing cells (right bars). **e)** Spatial distribution of anomalous exponents in nuclei of quiescent (e) and **f)** actively transcribing cells. **g) S**patial patterning of the anomalous exponent of the highly sub-diffusive population; color bar changed to range from dark blue to yellow for the anomalous exponent (slow group) between 0.3 to 0.73. The intermediate and high population are shown in light and dark red, respectively. Maps shown for quiescent (g) and **h)** actively transcribing cells.
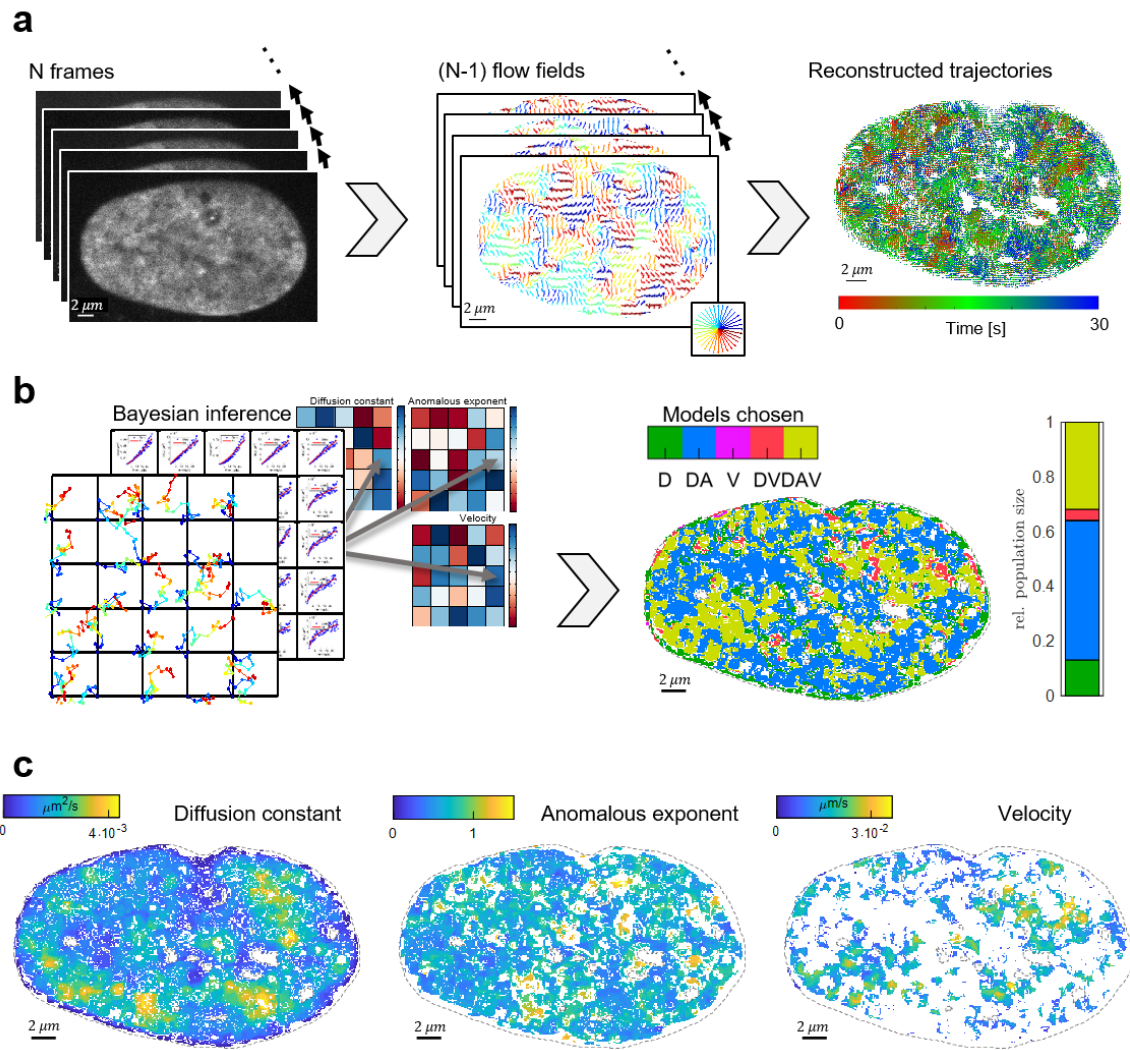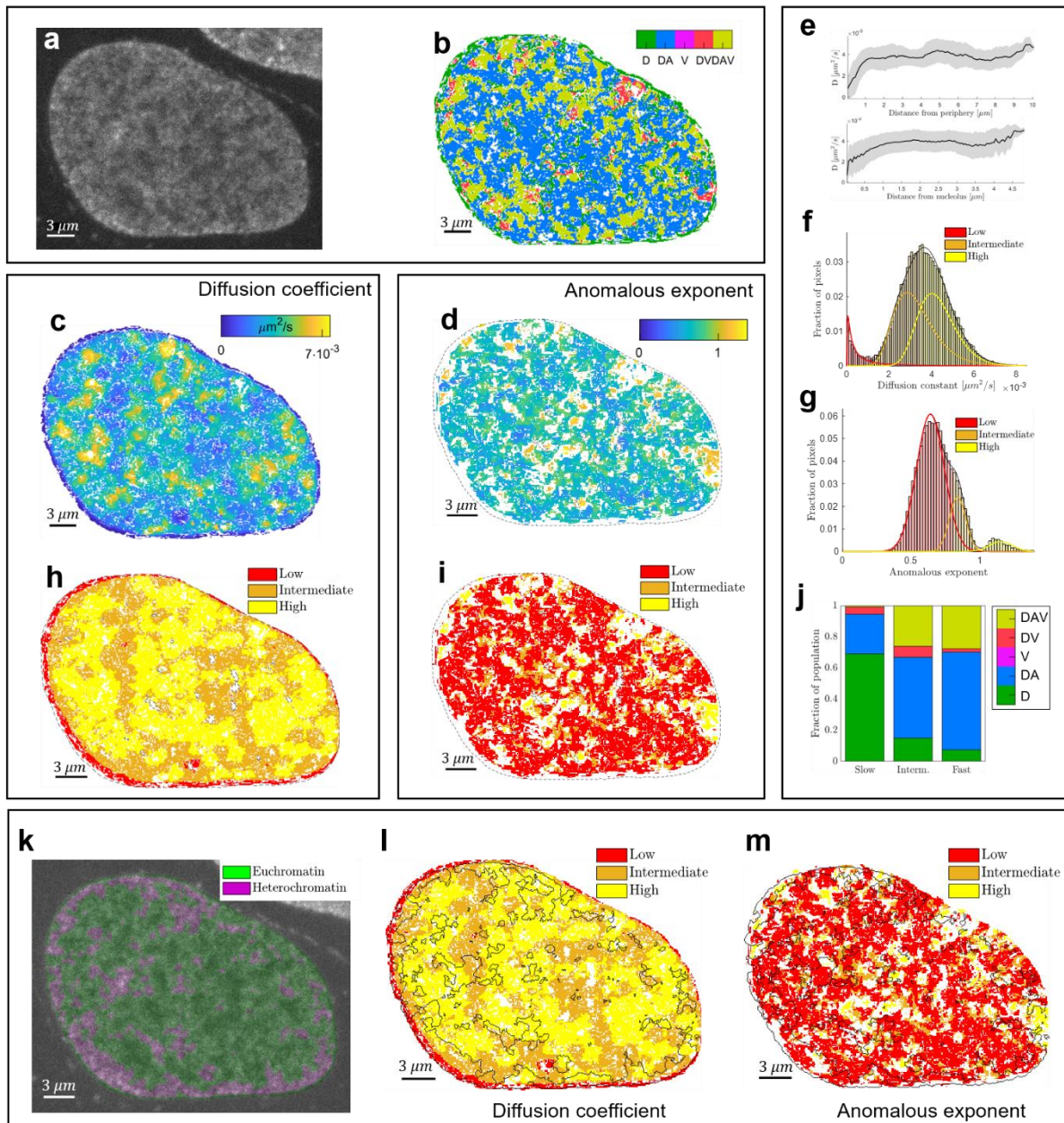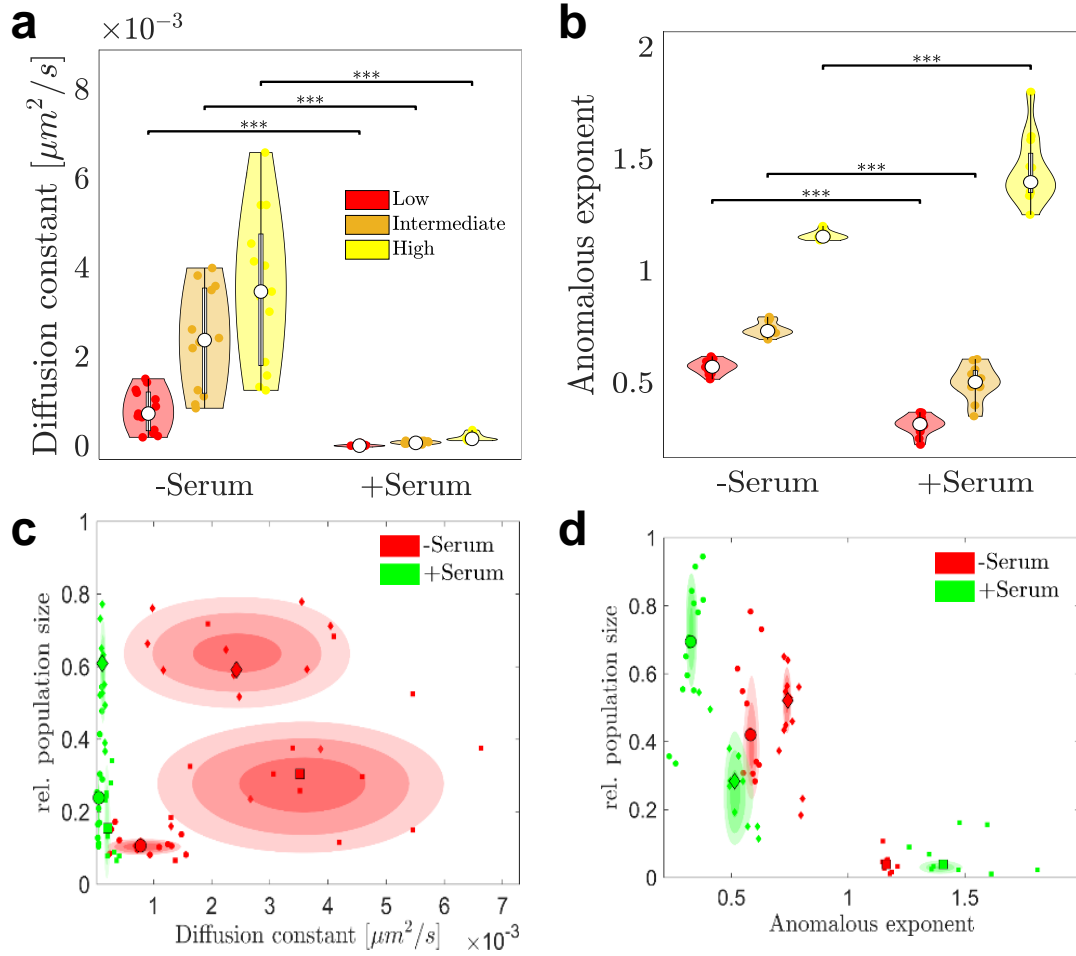
Figure 1

Figure 2

Figure 3

Figure 4